Mon. Not. R. Astron. Soc. **319**, 377–392 (2000)

N-body model for M51 – I. Multiple encounter versus single passage?

Heikki Salo★ and Eija Laurikainen
Division of Astronomy, Department of Physical Sciences, University of Oulu, PO Box 3000, FIN-90014 Oulun yliopisto, Finland

Accepted 2000 April 4. Received 2000 March 24; in original form 1999 October 6

ABSTRACT

A numerical survey of the encounter history of the interacting grand-design system M51 (NGC 5194/5195) is performed with a 3D multiple spherical polar grid code, where both components of the pair are described with self-gravitating star + gas discs embedded in rigid analytical halo potentials. Two classes of models are investigated, (1) nearly parabolic single passages, and (2) bound encounters implying several disc-plane crossings. Both types of models can approximate the general morphology of the M51 system and simultaneously fit the projected velocity difference and separation of the components. In both cases the companion disc-plane crossing responsible for the main spiral structure occurred nearly in the south, about 400–500 Myr ago at a distance of 25–30 kpc, but in opposite directions. In the bound encounter model there is also a more recent crossing, at a distance of 20–25 kpc about 50–100 Myr ago.

Our models account for some important kinematical observations of the M51 system not explained by the previous models. Especially, we note that the multiple-encounter model with a recent passage produces significant out-of-plane velocities, which manifest as an S-shaped structure of the major axis rotation curve, and which also explain the high peculiar velocities in the north of the companion. In this model the resulting extended tail is tilted 40°–50° with respect to the inner disc, leading to a velocity field that appears to suggest counter-rotation of the tail with respect to the inner disc. Also some morphological features, like the direction of the tidal extensions from the companion, are better matched by a model with a recent encounter. Importantly, any pre-existing spiral arms are washed out by the tidally triggered spiral arms.

The multiple-encounter model assumes a high inclination ($i \approx 85°$) orbit, with a low *current* eccentricity ($\epsilon \approx 0.2$). The possible origin of this type of bound orbital configuration is studied by simulations including the orbital decay via the Chandrasekhar formula for dynamical friction, and also by simulations including a self-consistently modelled live halo for the primary. The gross features of the model, including the tilted far tail, are preserved even when allowing for the effects of several earlier passages. The observed well-defined far tail seems to suggest that the previous passages have been at least 30 per cent more distant than the latest two crossings. According to our limited orbital survey, such an orbital decay can be accounted for, provided that M51 has an extended dark halo containing at least a few times the mass within the visible disc region (total $M_{\rm halo}/M_{\rm disc} \sim 10$).

Key words: galaxies: individual: M51 – galaxies: interactions – galaxies: kinematics and dynamics – galaxies: spiral – galaxies: structure.

1 INTRODUCTION

The formation and maintenance of global spiral structure in grand-design galaxies has been in the focus of interest since the landmark paper by Lin & Shu (1964), who introduced the density-wave theory based on a quasi-stationary spiral structure. This picture of arms as rigidly rotating density enhancements offers a plausible explanation for the survival of moderately open spirals despite differential rotation, which would wind up any material arms in just a few galactic revolutions. M51, with two prominent global spiral arms, provides a good example of density waves in the stellar component, and it has been one of the first test cases for the Lin–Shu density wave theory (Tully 1974c; Shu, Stachnik & Yost 1971). On the other hand, M51 obviously has a close companion, NGC 5195, which has inspired numerous efforts to explain its spiral structure by tidal effects. Toomre & Toomre

★ E-mail: heikki.salo@oulu.fi

made the first test particle simulations for M51, presented in their classical 1972 paper (Toomre & Toomre 1972, hereafter TT72). Their nearly parabolic orbit reproduced well the bridge and tail morphology of M51 as known at that time. TT72 suggested that many currently interacting galaxies may be systems on marginally bound relative orbits, instead of representing random hyperbolic passages. However, in their view, for example, the M51 system is currently experiencing its first close passage.

In TT72 a nearly parabolic ($\epsilon = 0.8$), high-inclination (75°) passage of the companion was assumed, with the disc-plane crossing and pericentre passage taking place in the north-west quadrant about 100–200 Myr ago: the mass of the companion was 1/3 of the primary. The model reproduced also the faint tidal extensions emanating from the companion in the approximately east–west directions. The lack of the main spiral structure was attributed to the neglect of self-gravity, as later supported by Zang's (1976) self-gravitating simulation with a 2D polar code, and by Toomre's (1981) demonstration of how swing amplification in the inner disc can magnify tidally induced weak kinematic waves. Hernquist (1990) made the first fully self-consistent 3D treecode simulations for M51, concentrating on parabolic relative orbits. His study emphasized that besides the inclusion of self-gravity, a considerably longer duration of the perturbation is required for the formation of the extended H I tail, discovered by Rots et al. (1990). In Hernquist's most successful experiments, the time since the crossing was about 2–3 times longer than in the TT72 model: this longer duration required pushing the crossing direction to the south-west. Compared to TT72, he also reduced the pericentre distance and increased the companion mass to one half. His model explains qualitatively the main spiral pattern and the extended H I tail, but was not able to match well simultaneously the galaxy morphology and the velocity difference between the galaxies. More recently, Toomre has refined the TT72 original model by including the disc self gravity and by allowing the crossing to occur at nearly south of the primary, with a correspondingly increased duration since the perturbation (Toomre 1995; see also Barnes 1998). By adopting the mass ratio of unity, quite a successful morphological match can be obtained, the extended H I tail being particularly well reproduced.

However, as discussed by Barnes (1998), the understanding of the M51 system is still far from being satisfactory, especially with reference to the apparent counter-rotation in the extended H I tail, which most likely indicates considerable tilt with respect to the inner disc of M51 (Rots et al. 1990). This is difficult to account for by the above mentioned models. Also, contrary to observations, the tidal debris from the companion spreads in approximately a north–south direction if the perturbation takes place near the south. A problem in the Toomre (1995) model is also the assumed very large companion mass. A possible solution for these problems is that the present structure of M51 manifests more than one close encounter, implying a low current eccentricity for the orbit. A similar bound orbital configuration has been suggested for another M51-type interacting galaxy pair, NGC 7753/52, by Salo & Laurikainen (1993; hereafter SL 93).

An interesting additional observation has been the central spiral structure of M51, discovered by Zaritsky, Rix & Rieke (1993) in the *K*-band. These stellar spirals, winding 1.5 revolutions inside 30 arcsec, ending in a central oval, form a smooth continuation of the main spiral structure. Although the main spiral structure seems to be well described by tidal models, without need for help from intrinsic modes, it is currently unknown whether external perturbation could be able to excite these innermost structures.

In the present study we investigate single- and multiple-passage orbits for M51 system, and present simulation models which appear to match many of the observational characteristics of the system. The simulations, described in Section 2, are performed with a 3D spherical polar grid code and include the disc self-gravitation, while in most runs the spherical component is described with an analytical potential model. In Section 3 we study the different models: we compare in detail the morphological and kinematical implications of the multiple-passage versus single-passage models. The possible origin of the bound orbital configuration is explored in Section 4, both by using the semi-analytical method with the Chandrasekhar formula for dynamical friction and also by fully self-consistent simulations with live haloes. In Section 5 we collect and discuss the main results. In the next paper (Salo & Laurikainen 2000; hereafter Paper II) we will concentrate on the innermost structure of M51, and also analyse in more detail the properties of the tidally induced waves.

2 SIMULATION METHOD AND INITIAL MODELS

2.1 Simulation method

The simulations are carried out with a 3D multiple-grid code, based on the use of overlapping comoving logarithmic spherical polar grids for the potential evaluation, combined with a Cartesian centre-of-mass orbital integration. Both components of the interacting pair are described with self-gravitating star + gas discs embedded in analytical spherical haloes. The coordinate grids are centred on the halo centres and the disc back-action is taken into account in the halo motion. Experiments with self-consistent haloes are also performed, as described in more detail in Section 4. Moving logarithmic spherical grids offer efficient means for the evaluation of the self-gravity of the disc via fast Fourier transformation, and give good spatial resolution in the inner parts of both systems. A short description of the 3D code can be found in SL93, while a full description of its 2D version was given in Salo (1991).

In the present study we use density/potential grids with $N_R = 48$ radial, $N_\phi = 36$ azimuthal, and $N_\theta = 19$ latitudional cells, implying 10° resolution. The grid extends from 1 to about 3600 arcsec, covering well the region of interest (size of the extended tail is about 900 arcsec). The gravitational potential is further smoothed by using an explicit gravity softening, amounting to $\epsilon = 20$ arcsec or 0.05 simulation units (1 simulation unit is 400 arcsec). The integration time step is 0.01 outer disc crossing times, ensuring at least 20 steps/orbital revolution even in the innermost portions of the discs. The stellar discs are represented by $N_{\rm star} = 200\,000$ and 60 000 particles for the primary and the companion, respectively. This rather coarse resolution and small $N_{\rm star}$ are sufficient for the study of the gross features excited by tidal perturbation. In Paper II, dealing with the inner structure, especially the central spirals observed within 30 arcsec (Zaritsky et al. 1993), and the details of the formation of tidal arms, a better grid resolution in combination with a smaller gravity softening is used, together with a much-increased $N_{\rm star}$.

The difference in the treatment of star and gas particles is that the latter have a finite cross-section and experience dissipative collisions ('sticky particle' method). In each impact, the component of the relative velocity in the direction joining the particle centres is reversed and reduced by a factor α. In the current study

we set $\alpha = 0$, and use $N_{\rm gas} = 50\,000 + 15\,000$ gas particles, with radii of 0.0005 in the simulation units. With these parameter values, the gas radial velocity dispersion attains a rough equilibrium of 5–10 km s^{-1} when the system is evolved in isolation: this is comparable to that found for our Galaxy. The same method for the treatment of the gas component has been used in our recent modelling of the barred galaxy IC 4214 (Salo et al. 1999), as well as in producing gas velocity fields for magneto-hydrodynamical simulations of the same system (Moss, Rautiainen & Salo 1999).

2.2 Disc and halo models

For the orientation of the disc of NGC 5194 we adopt Tully's (1974a,b) kinematical estimates, $\mathrm{PA_{disc}} = 170^\circ$ and $i_{\rm disc} = 20^\circ$ (eastern side is tilted toward the observer). For the companion, lacking any overall spiral structure, the estimates are much more uncertain. We adopt $\mathrm{PA_{disc}} = 90^\circ$ (Schweizer 1977; Smith et al. 1990) and $i_{\rm disc} = 30^\circ$ (Smith et al. 1990). Assuming that the northern side of the companion is tilted toward the observer, these values yield a relative inclination of 32.5° with respect to the disc of M51.

The surface density of the disc is described by the exponential profile,

$$\Sigma(r) = \begin{cases} \Sigma_0 \exp(-r/R_{\rm e}), & r \le R_{\rm d}; \\ 0, & r > R_{\rm d} \end{cases} \qquad (1)$$

where $R_{\rm e}$ is the scalelength and $R_{\rm d}$ the truncation radius of the disc. The constant Σ_0 is related to the total mass contained within $R_{\rm d}$, $M_{\rm disc} = 2\pi\Sigma_0 R_{\rm e}^2[1 - (1 + R_{\rm d}/R_{\rm e})\exp(-R_{\rm d}/R_{\rm e})]$. In the vertical direction, the initial distribution follows the isothermal sheet model (Spitzer 1942),

$$\rho(z) = \rho_o \,\mathrm{sech}^2(z/z_0), \qquad (2)$$

where $z_0 = \sigma_z^2/2\pi G\Sigma$ and σ_z is the vertical velocity dispersion. The amount of random velocities is determined by specifying the value of the Toomre's stability parameter, $Q_{\rm T} = \kappa\sigma_{\rm r}/3.36G\Sigma$, where κ is the epicyclic frequency and $\sigma_{\rm r}$ is the radial velocity dispersion: as a standard value we use $Q_{\rm T} = 1.5$. Initial random velocities follow Gaussian distribution, and the ratio of radial to tangential velocity dispersion is calculated from the epicyclic approximation, $\sigma_{\rm r}/\sigma_{\rm t} = 2\Omega/\kappa$. The circular velocities are corrected for the pressure support by random velocities, with the asymmetric drift equation (Binney & Tremaine 1987, p. 202). The ratio of vertical to radial velocity dispersion $\sigma_z/\sigma_{\rm r}$ is taken to be 0.7 throughout the disc.

We adopt $R_e = 100$ arcsec for the initial scalelength of the stellar disc of M51, which is close to the observed scalelength of 95 arcsec (Schweizer 1976). In the outer parts (>150 arcsec), the azimuthally averaged brightness has a considerably steeper slope. Simulations indicate that this modification can arise as a result of the interaction, so that the use of the single exponential initial profile is justified. The truncation of the disc is set to $R_{\rm d} = 4R_{\rm e} = 400$ arcsec. A similar distribution is used for the gas component.

The observed light distribution of the companion is exponential for $r <$ 70–90 arcsec, beyond which it is extremely flat (Smith et al. 1990; Thronson et al. 1992; Spillar et al. 1992). It is possible that the disc of the companion has undergone drastic changes during the interaction. For example, as pointed out by TT72, deep exposures (Burkhead 1978) display material to the north-west and south-east of the companion, most probably representing the tidal bridge and tail originating from the companion. In order to reproduce these features, TT72 adopted a fairly extended disc, with an outer radius 70 per cent of that for the primary. We make a similar assumption and take $R_{\rm d} = 240$ arcsec $\approx 7R_{\rm e}$ for the initial companion disc, assuming $R_{\rm e} = 33$ arcsec ($R_{\rm e}$ in agreement with observations by Spillar et al. 1992).

For the analytical spherical haloes, isothermal sphere with a smooth transition to constant core density is used, described by a rotation curve

$$v_{\rm h}(r) \propto \sqrt{\frac{r^2}{r^2 + R_{\rm c}^2}}, \qquad r < R_{\rm h}, \qquad (3)$$

where $R_{\rm c}$ and $R_{\rm h}$ are the radius of the constant density core and the halo truncation radius, respectively. This simple model gives the main features of typical rotation curves: inside $R_{\rm c}$ it yields a linearly rising part, which then turns flat between $R_{\rm c}$ and $R_{\rm h}$, outside which Keplerian rotation is obtained.

The observed rotation curve of NGC 5194 (Tully 1974b; Tilanus & Allen 1991; Rand 1993) rises rapidly within 20 arcsec and reaches a maximum of about 220 km s^{-1} at the distance of 200 arcsec, decreasing gradually after that. As will be shown in Section 3, the decrease of velocities beyond 200 arcsec can be accounted for by the interaction, and therefore we use an initial rotation curve which is essentially flat also for $200 < r <$ 400 arcsec. In all the experiments in this paper we assume that $M_{\rm disc}/M_{\rm tot} = 1/3$ within $4R_e$. For this mass ratio, the choice of $R_{\rm c} = 8$ arcsec gives a reasonable fit to the innermost part of the rotation curve. The halo truncation is set at $R_{\rm h} = 400$ arcsec, except in Section 4, where the effects of a more extended halo are studied.

In most of the runs we use $M_{\rm p} = M_{\rm tot}({\rm comp})/M_{\rm tot}({\rm prim}) = 0.55$, which is somewhat larger than the observed disc mass ratio ≈0.4 (Schweizer 1977; Smith et al. 1990). However, the use of a larger mass ratio is motivated by the fact that small galaxies are likely to have more dominant halo components: according to Persic & Salucci (1990), $M_{\rm halo}/M_{\rm disc} \propto L_{\rm disc}^{-0.5}$. We thus set for the companion $M_{\rm disc} = 0.13$ and $M_{\rm halo} = 0.42$, consistent with the above relation and the assumed disc-to-halo ratio for the primary. The truncation radius of the companion halo is set equal to the disc truncation, $R_{\rm h} = 240$ arcsec. For the constant density core we use $R_{\rm c} = 40$ arcsec, reflecting the lesser degree of halo concentration expected for smaller galaxies.

2.3 Simulation units and orbital constraints

In the simulations, scaled units are used by setting $GM = 1$ and $R_{\rm d} = 1$, where M is the total mass within the truncation radius of the primary disc, $R_{\rm d}$, and G denotes the gravitational constant. Therefore, the circular velocity at $R_{\rm d}$ is also close to unity. In these units the disc mass is fixed to 1/3. We take the length unit = 400 arcsec = 18.6 kpc, and the velocity unit = 220 km s^{-1}, so that one mass unit $\approx 2 \times 10^{11}$ M$_\odot$. Here we have assumed the distance of 9.6 Mpc for M51 (Scoville & Young 1983). The time unit (equal to the crossing time at the edge of the primary disc) corresponds to 18.6 kpc /220 km s^{-1} $\approx 80 \times 10^6$ yr. This time unit is used throughout the paper, whereas in most of the plots we use angular units for distances and km s^{-1} for velocities.

The position of M51 is taken to be $\alpha_{1950} = 13^{\rm h}27^{\rm m}46\overset{\rm s}{.}3$, $\delta_{1950} = 47°27'10''$, which is the location of the central radio continuum source (Ford et al. 1985). For NGC 5195, $\alpha_{1950} = 13^{\rm h}27^{\rm m}53\overset{\rm s}{.}3$, $\delta_{1950} = 47°31'26''$ (Thronson et al. 1992). This implies separation $\Delta\alpha \approx 70'' = -0.176$ simulation units and $\Delta\delta = 255'' = 0.639$

simulation units. In the models we attempt to match this projected separation as accurately as possible. In most of the preliminary experiments we used the velocity difference of $\Delta v = 100\,\mathrm{km\,s^{-1}}$ for the components, in agreement with the observations by Appleton, Foster & Davies (1986). However, in the final models $\Delta v \approx 110$–$130\,\mathrm{km\,s^{-1}}$, consistent with the velocity measurements by Schweizer (1977).

3 SINGLE ENCOUNTER VERSUS MULTIPLE ENCOUNTER

3.1 Initial orbital search

In order to study the possible encounter histories of the M51 pair, an extended survey of several hundreds of self-gravitating simulation experiments has been performed, with various orbital geometries and perturber masses. All of these experiments start with initial values which lead to orbits fulfilling the relative separation and velocity difference constraints with good accuracy. This is achieved with the orbital fitting procedure, described in detail in SL93: we first specify the location of the primary disc-plane crossing and the elapsed time since that event. The use of disc crossing instead of pericentre passage is motivated by the high inclination of the relative orbit. Then we search iteratively, with the Powell method, the initial values of the companion orbit that will pass through the present projected position with the right velocity difference. Each such iteration step involves integration of the companion orbit: these integrations are very fast, as they include only the analytical halo potentials and the fixed axisymmetric disc potential of the primary. Provided that the

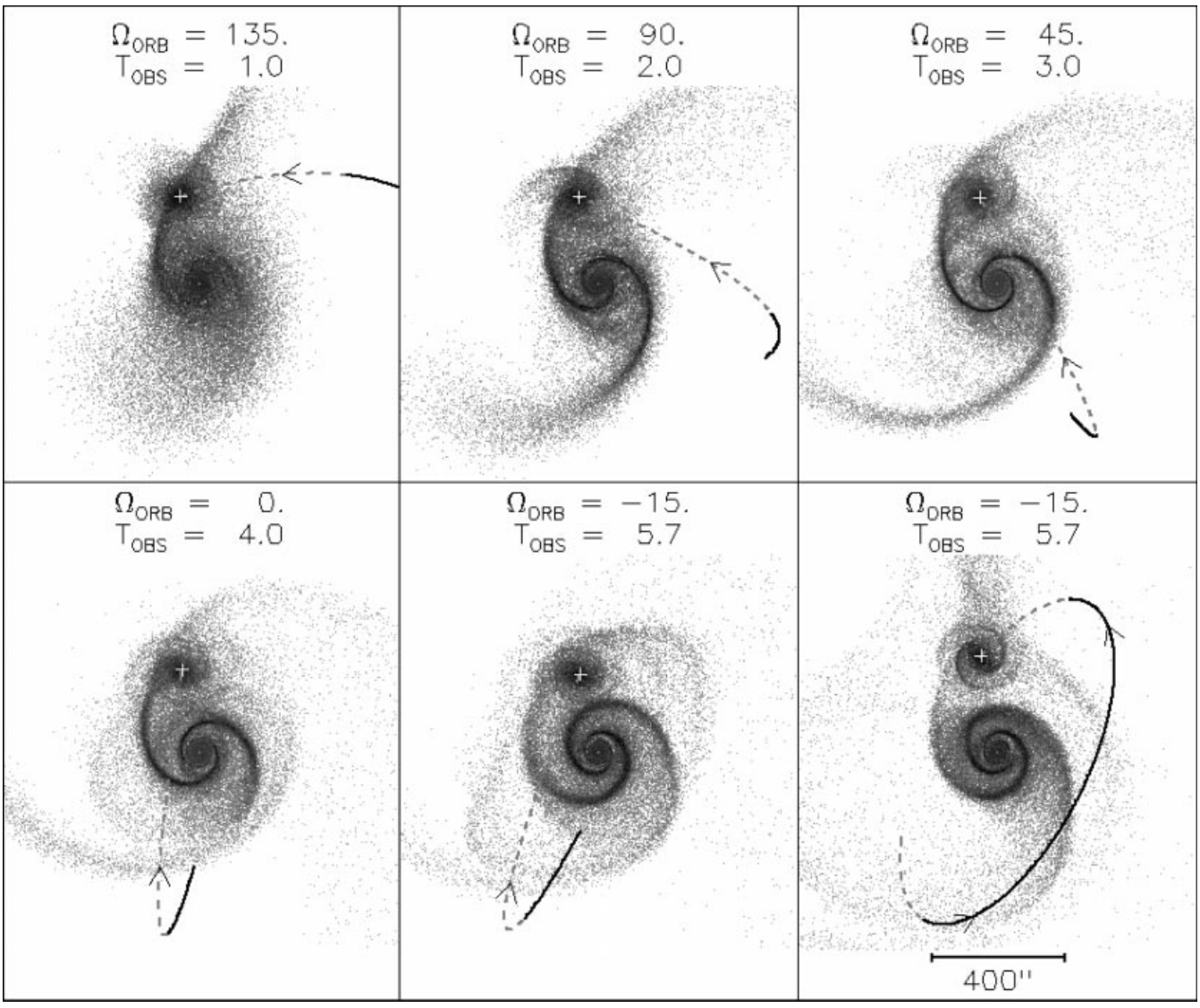

Figure 1. Sequence of M51 experiments, with an increasing duration since the principal perturbation (companion crossing of the primary disc plane). In each case the perturber to primary mass ratio, $M_\mathrm{p} = 0.55$ and the disc-plane crossing occurred at $R_\mathrm{cross} = 1.4$. The projection of the simulation gas particles to the observing direction is displayed (PA $= 170°$, $i = 20°$), together with the relative companion orbit: dashed lines correspond to the portion behind the primary disc. Numbers in the frames indicate the azimuth of the disc crossing (equal to Ω_orb), counted ccw along the disc plane from the intersection with the sky-plane at PA $= 170°$, and the time T_obs elapsed since the disc plane crossing at $T = 0$. For the last frame, the orbit crosses the plane of the primary twice, and the azimuth of the first crossing is given. All simulations started at $T_\mathrm{start} = -1.0$. Except for the last frame, the orbits have high eccentricity ($\epsilon = 0.67$–0.83) while the inclination $i_\mathrm{orb} \approx -75°$: for the last case $\epsilon = 0.2$ and $i_\mathrm{orb} = 85°$. For the single-passage orbits, the pericentre is close to disc crossing; in the multiple-passage model the apocentre is between the two disc crossings.

disc deformation is not too strong, the method also usually provides tolerable accuracy of the position and velocity fit in the final self-gravitating model, in which both the self-gravity of the discs and their back-action on haloes are included. In this manner we can study systematically the variations caused in both the present morphology and the velocity features, arising from different perturbation strengths and passage ages. However, since the simulations presented in this section employ analytical haloes, they do not properly include the orbital decay arising from dynamical friction. The results are thus applicable only to the latest portion of the relative orbit, and even then with only finite accuracy.

Fig. 1 displays an example of the orbital search runs, performed with a fixed primary perturbation (highly inclined disc crossing at $R_{\rm cross} = 1.4$ and $M_{\rm p} = 0.55$), but increasing the elapsed time $T_{\rm obs}$ between the disc crossing and the present time. Increasing $T_{\rm obs}$ requires pushing the crossing azimuth further and further to the south, so that the bridge can attain its observed location. In each case the projected location of the companion agrees with the observed one within the accuracy of 15 arcsec and the radial velocity difference corresponds to $100\,{\rm km\,s^{-1}}$ within about 5 per cent.

The encounter displayed in the first frame of Fig. 1 is close to the TT72 original model, while those in the fourth and fifth frames resemble the model by Toomre (1995), except that because of the smaller perturber, our tail is less extended. We can see that by increasing the duration of the perturbation, a good resemblance with the observations is achieved by these nearly parabolic, single encounters, in agreement with the tree-code simulations of Hernquist (1990). On the other hand, the last frame shows an example of another possible orbital family, in which the principal perturbation again occurs to the south of the primary disc, but in this case the companion velocity is toward the observer. The much smaller eccentricity of the orbit allows the companion to cross the primary disc a second time, so that it can attain its current position and velocity away from observer. Extended surveys with different values of $R_{\rm cross}$ and $M_{\rm p}$ show that both types of orbital solutions are possible for a rather wide range of parameters: for example larger $R_{\rm cross}$ can be compensated by slightly larger $M_{\rm p}$.

3.2 Single or multiple passage?

How to distinguish observationally between these two families of solutions? With suitable fine-tuning, a good overall morphological match can be found by both types of orbits (see Toomre 1995; Salo & Byrd 1994; Byrd & Salo 1995). However, the direction of the perturbation in the southern disc plane passage is opposite in the two types of models, which manifests on the kinematical properties of the models, especially on the direction of the out-of-plane velocities in the outer disc. Secondly, the multiple-passage model implies a second, recent disc-plane crossing and therefore a strong current perturbation, whereas in the single encounter model the perturber is already so far behind the primary galaxy that its current influence is negligible. We will first look at the possible morphological evidence of the recent crossing and then compare the kinematical features in the two types of models.

3.2.1 *Morphological support for a recent perturbation*

Fig. 2 displays the large-scale morphology of the multiple-passage model, in comparison with the digitized Palomar Observatory Sky Survey (POSS) image. The lower panels show the simulated star particles separately for the main galaxy and the companion. Clearly visible are the streamers in the north of the companion, composed of material drawn from the primary galaxy, and the tidal extensions originating from the companion. Both of these features have counterparts on the POSS image, and arise naturally in the multiple-passage model as a result of the recent passage. The morphology of the tidal debris from the companion is very similar to that in the TT72 model, as can be expected since our companion disc has an extent similar to that used in their simulations, and also since our most recent disc crossing occurs roughly at the same time and in the same direction as the single passage in the TT72 model. On the other hand, in our single-passage models, the tidal debris from the companion has practically totally dispersed at the present time as a result of the long duration since the principal perturbation. Note that the companion has developed a small bar during the interaction (in isolation the companion model is stable against bar formation). In the experiment shown, the bar orientation matches quite closely the observed alignment toward the primary galaxy. This is, however, model dependent, as the bar pattern speed and thus its orientation at a given time depends on the rotation curve assigned to the companion.

Elmegreen, Elmegreen & Seiden (1989) first pointed out the presence of two almost symmetrically located 'kinks' in the spiral arms of M51, at distance of about 140 arcsec. The northern 'kink' close to the companion is especially pronounced. It is tempting to identify this 'kink' as another possible signature of a recent perturbation. In the multiple-encounter model, this kind of feature forms naturally via the recent perturbation on the spiral arm, provided that the distance of the recent disc plane crossing is small enough (see Fig. 2). On the other hand, for the main spiral structure, the effect of the recent perturbation is insignificant.

3.2.2 *Kinematical support for the multiple-passage model*

The visible disc of M51 is surrounded by a large extended H I tail, discovered by Rots et al. (1990). High-velocity gas is also seen in the north of the companion. The extended H I tail shows anomalous kinematic behaviour: the maximal velocities toward the observer are seen at PA $\approx 155°$, compared to PA $= -10°$ for the inner disc. This suggests that the plane of the extended tail must be tilted to the opposite side of the sky plane as compared to the inner disc. Indeed, Rots et al. (1990) estimated this tilting to be about 40°. The H I emission north of the companion has velocities amounting to $250\,{\rm km\,s^{-1}}$ with respect to the central velocity of M51 ($460\,{\rm km\,s^{-1}}$). Most likely both of these peculiarities are associated with the interaction.

Fig. 3 compares the evolution of single and multiple-encounter models in more detail, both seen as projected to the sky, and along the disc plane of the primary. In the multiple-passage model, the initial velocity impulse given for the original tail particles is 'downward' (to the side away from the observer). These tail particles are perturbed into inclined, eccentric orbits: at the present time, about half of an orbital revolution later, at least part of them are moving 'upward' (to the side toward the observer) with respect to the original disc plane. As seen in the edge-on projection, the tilt of the tail is 40°–50°, being well in agreement with the observations by Rots et al. The simulated tail is actually composed of two distinct particle streams, the inner one originating from the particles of the initial bridge. Interestingly, most of these particles are currently turning 'upward', in spite of their initial 'upward' impulse: as they originated from somewhat deeper inside the disc than the tail particles, they have already

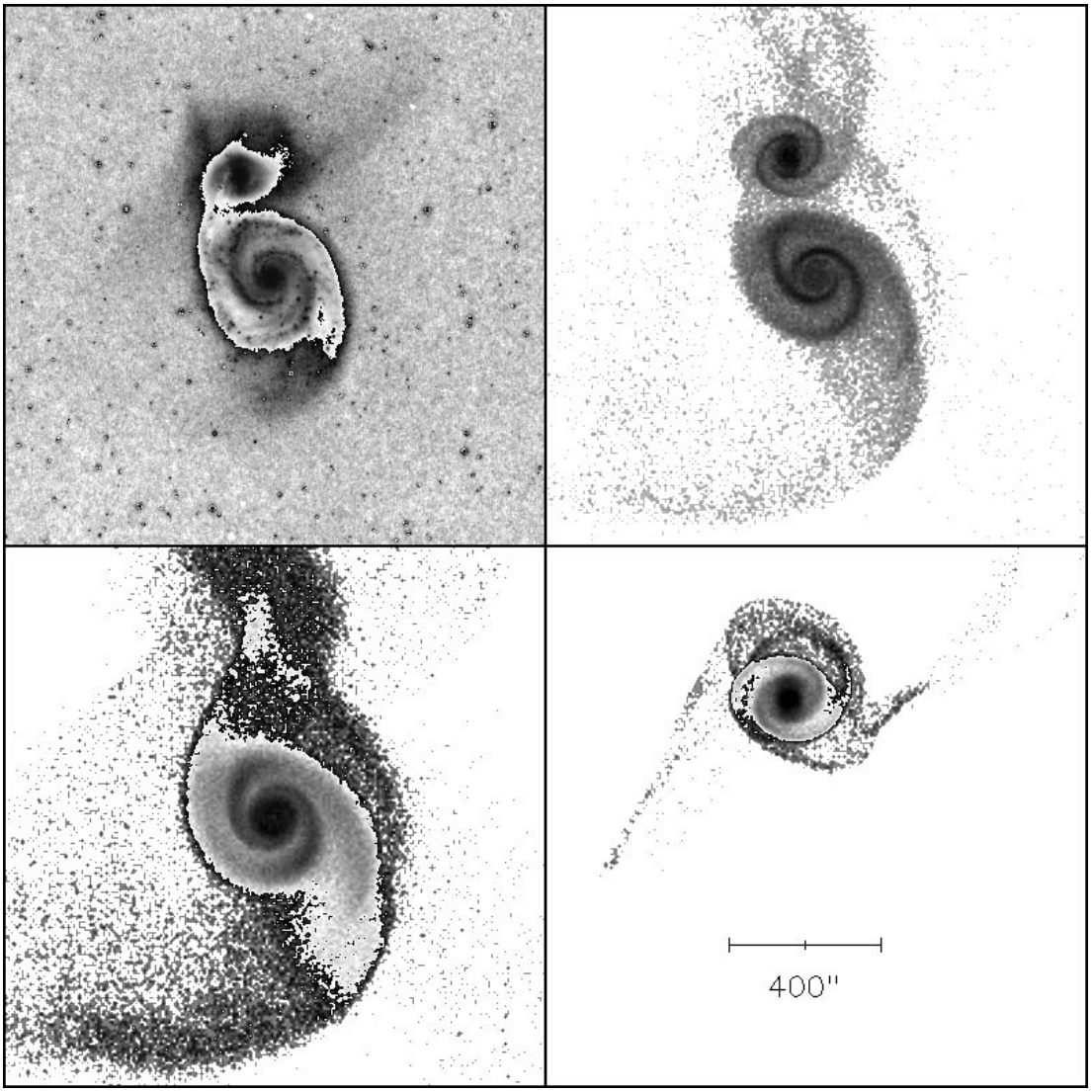

Figure 2. Extended morphology in the multiple-encounter model, compared with the digitized POSS image. In the lower left-hand frame, star particles originating from the primary galaxy are shown, while in the lower right are shown star particles originating from the companion. The upper right-hand frame is a combined plot of all simulation gas particles. Compared to the multiple-encounter model of Fig. 1, the most recent crossing takes place at a slightly smaller distance (about 1.1 units as compared to 1.25), making the 'kink' toward companion more pronounced. For a deeper image of the M51 system, see Burkhead (1978).

completed almost a full revolution. Consequently, the sky projections of the current out-of-plane velocities for both components of the tail are the opposite of the projected tangential velocity arising from the systematic inner disc rotation. In the single-passage model the initial impulse and, consequently, the present out-of-plane velocities, are roughly opposite to those in the multiple-passage model or in observations. Also, because of the faster crossing velocity in the nearly parabolic orbit, the velocity perturbations are smaller than in the multiple-encounter model, accounting for smaller tilt of the tail.

Fig. 4 compares the velocity fields of the single and multiple-encounter models with the observed H I velocity field by Rots et al. (1990). In the multiple-encounter model the kinematics of the extended H I tail is at least qualitatively reproduced, its apparent counter-rotation following from the large tilt with respect to the inner disc as explained above. Moreover, the velocity gradient of the simulated tail is about 40–50 $\mathrm{km\,s^{-1}}$, comparable to observations. Also, although the tail velocities of the model are systematically about 40 $\mathrm{km\,s^{-1}}$ larger than in the observations, waiting for just a quarter of a crossing time would shift the minimum tail velocities below 400 $\mathrm{km\,s^{-1}}$, as observed. In comparison, in the single-passage model the extended tail velocites join rather smoothly to the inner disc velocity field, as could be anticipated from the smaller tilt of the tail. Another important characteristic in the multiple-encounter model is that the most recent passage induces a stream of high-velocity particles towards the north, with velocities in accordance with observations (up to about 700 $\mathrm{km\,s^{-1}}$). Note that, for example, a stronger single-passage would not help in producing either the high velocities in the north or the correct direction of the tilt of the H I tail.

Even the multiple-encounter model fails to reproduce the observed velocity field of the outer disc region just beyond the visible disc, exhibiting an about 50° counterclockwise shift in the zero-velocity line. However, in spite of its pronounced

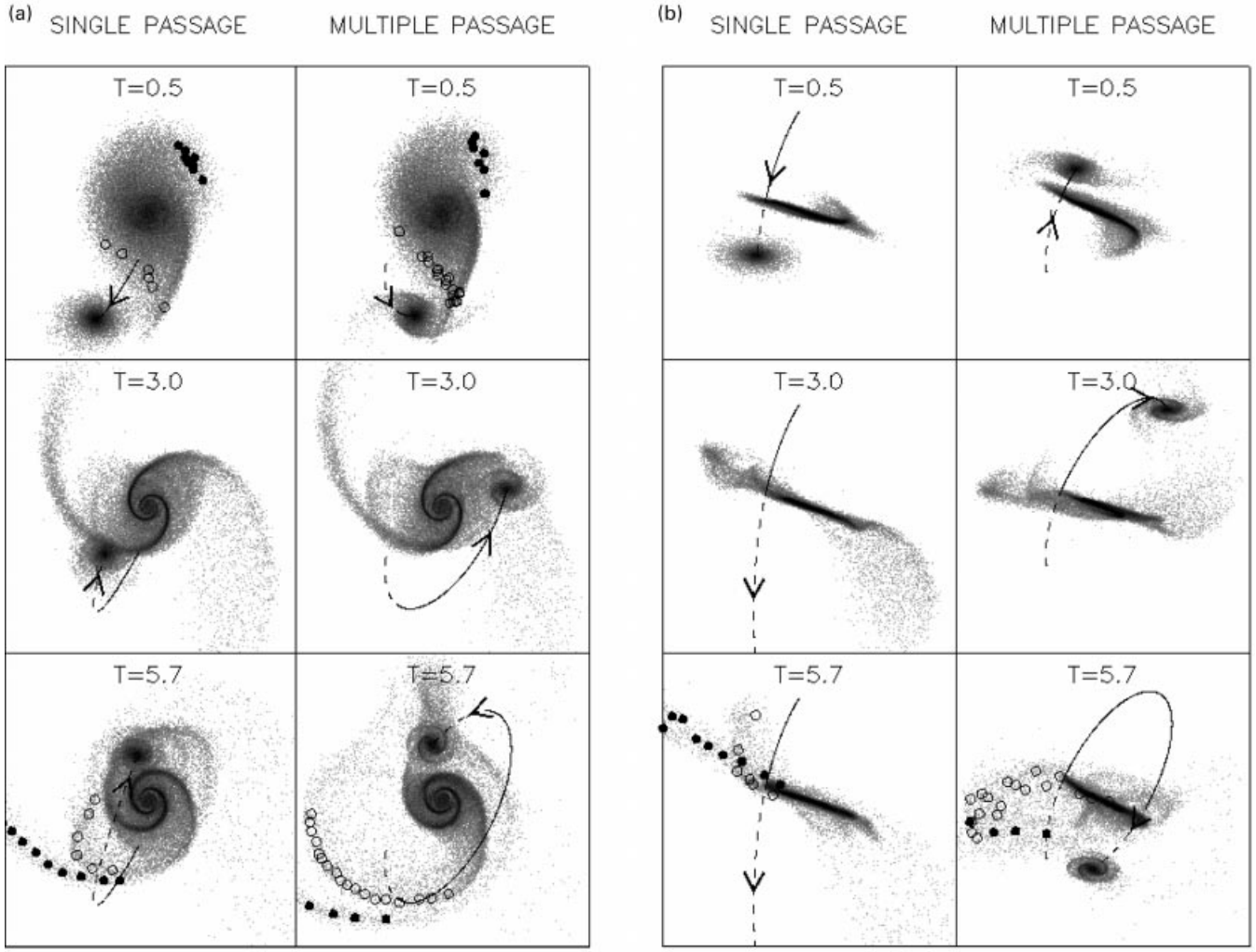

Figure 3. A more detailed comparison of the evolution in the single- and multiple-encounter models. The experiments correspond to the last two frames of Fig. 1. In (a) the projection to the sky plane is displayed, while (b) shows the edge-on view, looking approximately from south along the nodal line at PA = 170°. In order to explore the origin of particles in the extended tail region, some of its constituting particles are plotted by symbols: filled and open circles denote particles that originate from the initial tail and bridge, respectively. Notice the different z-direction of the current tails for the single and multiple-encounter models (to the left of the disc, corresponding to east in the sky). In the multiple-encounter model, the mean plane of the inner disc has been tilted about 5° as compared to the initial plane, so that the angle with respect to sky has become about 25°; in the single-passage model, the tilt is about 2° in the opposite direction, reducing the inclination with respect to the sky to about 18°.

appearence in Fig. 4 this feature is extremely weak. Also, in simulations there is some material in the north-west side of the primary disc, having no observational counterpart. The shift of the zero-velocity line could be an indication of still earlier passages, and their effects on the overall plane of the gas disc of M51.

Fig. 5 compares the major axis rotation curves for the multiple- and single-passage models. Also indicated are the circular velocity curves calculated from the mass distribution, as well as the observed major axis Hα rotation curve (Tilanus & Allen 1991). In the single-passage model, the rotation curve remains very similar to the circular velocity curve, except for the velocity shifts associated with the spiral arms. On the other hand, the multiple-encounter model gives a strong decline beyond about 200 arcsec, being especially pronounced in the north, in agreement with observations. The S-shaped rotation curve is mostly the result of significant out-of-plane velocities produced during the encounter, not of changes in the mass distribution. A smaller decline is also visible in the model where the companion was removed before the second passage.

3.3 Effect of a possible pre-encounter structure

The above models have shown that the assumed tidal encounter may reproduce the observed morphology. However, they have all started from a practically featureless initial state. As stressed by Lin & Bertin (1995), this is not a very realistic initial state. To check the possible influence of a pre-existing spiral structure, some additional experiments were conducted with initial models possessing moderately strong spirals before the perturbation was started. These spirals were created by subjecting the disc to an about 50 per cent weaker tidal perturbation, and then allowing this disc to evolve by about 10 time units, before the actual encounter model was started. Two models with pre-existing structure are shown in Fig. 6, and are compared to a model with an initially axisymmetric disc. According to these experiments, the assumed encounter geometry leads to such a strong perturbation that it is capable of overwhelming, almost completely, the signs of the pre-existing structures before the nominal observing time is achieved.

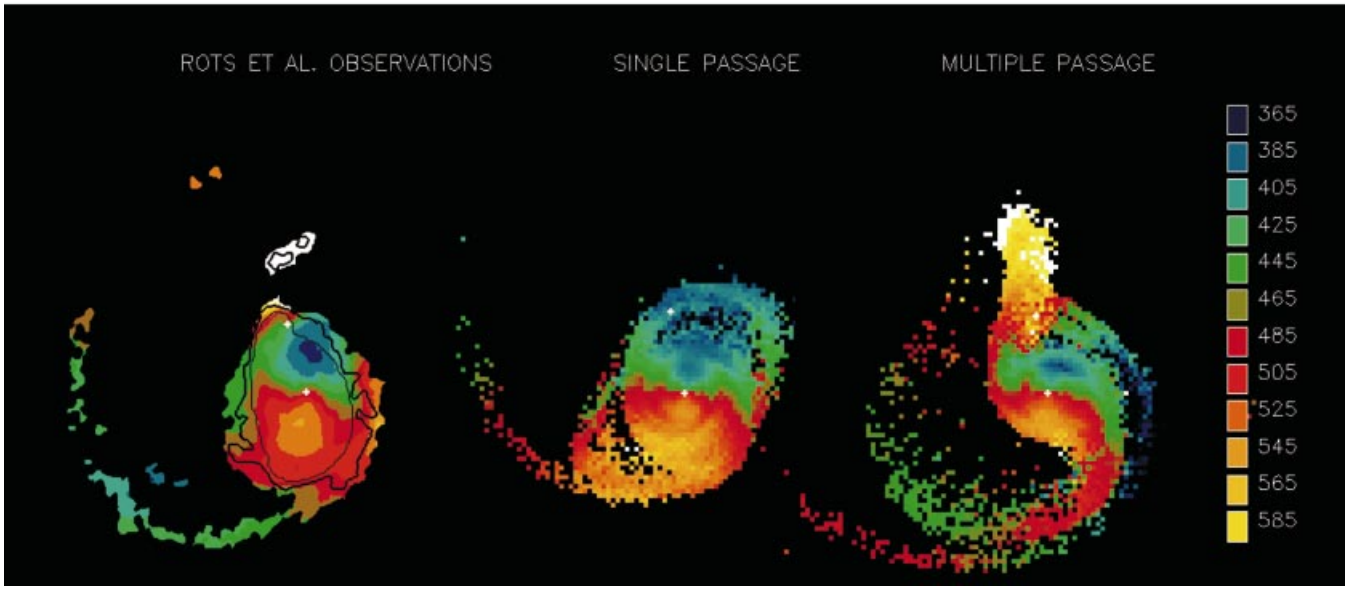

Figure 4. The comparison of the gas velocity field in single- and multiple-passage models (frames 5 and 6 in Fig. 1), together with the observed extended H I velocities. The observational data are taken from fig. 7 of Rots et al. (1990): the fourth and fifth density contours of their fig. 5 are overlaid on the velocity data. In simulations the slight tilting of the primary disc (see Fig. 3) during the interaction has been taken into account, and the viewing direction has been chosen so that the kinematic orientation of the inner disc corresponds to Tully's (1974a,b) values (PA = 170°, $i = 20°$).

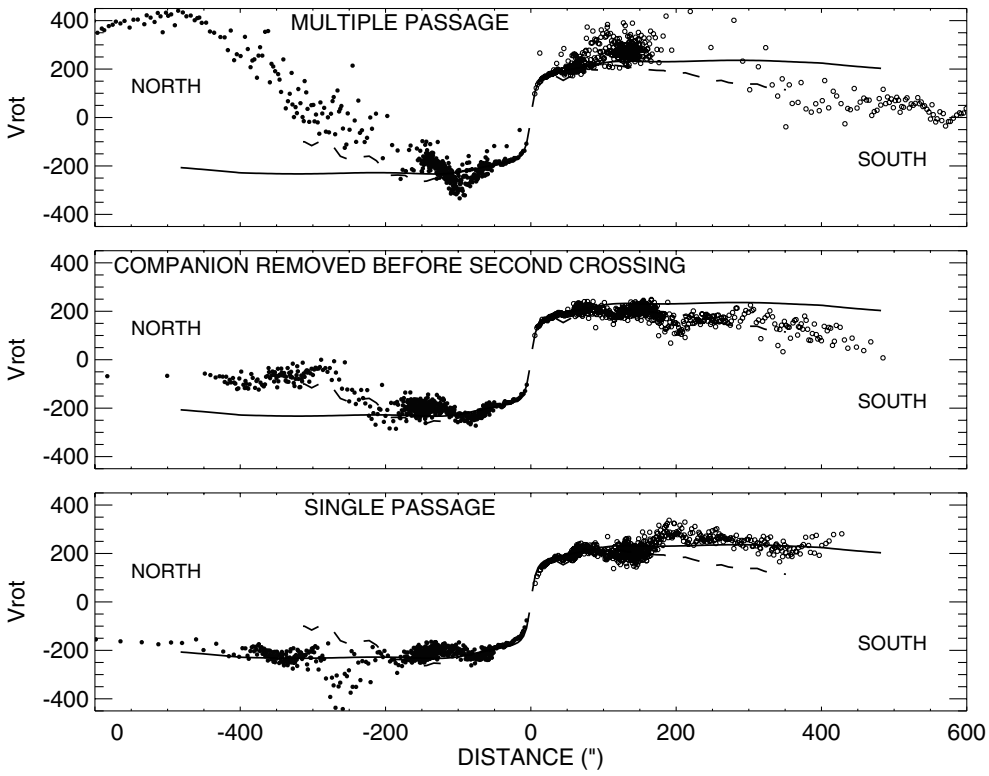

Figure 5. Comparison of the major axis rotation curves for the single- and multiple-encounter simulations of Fig. 1, at $T = 5.7$. Symbols denote the rotation velocities derived from the line-of-sight velocities, in a cone with a width of 40° around the kinematic major axis. The solid lines denote the circular velocity curves calculated from the mass distribution. The measured major axis Hα velocity curve (Tilanus & Allen 1991) is denoted by dashed lines. The experiment in the middle row is similar to the multiple-passage model of the first row, except that the companion has been removed at $T = 3$.

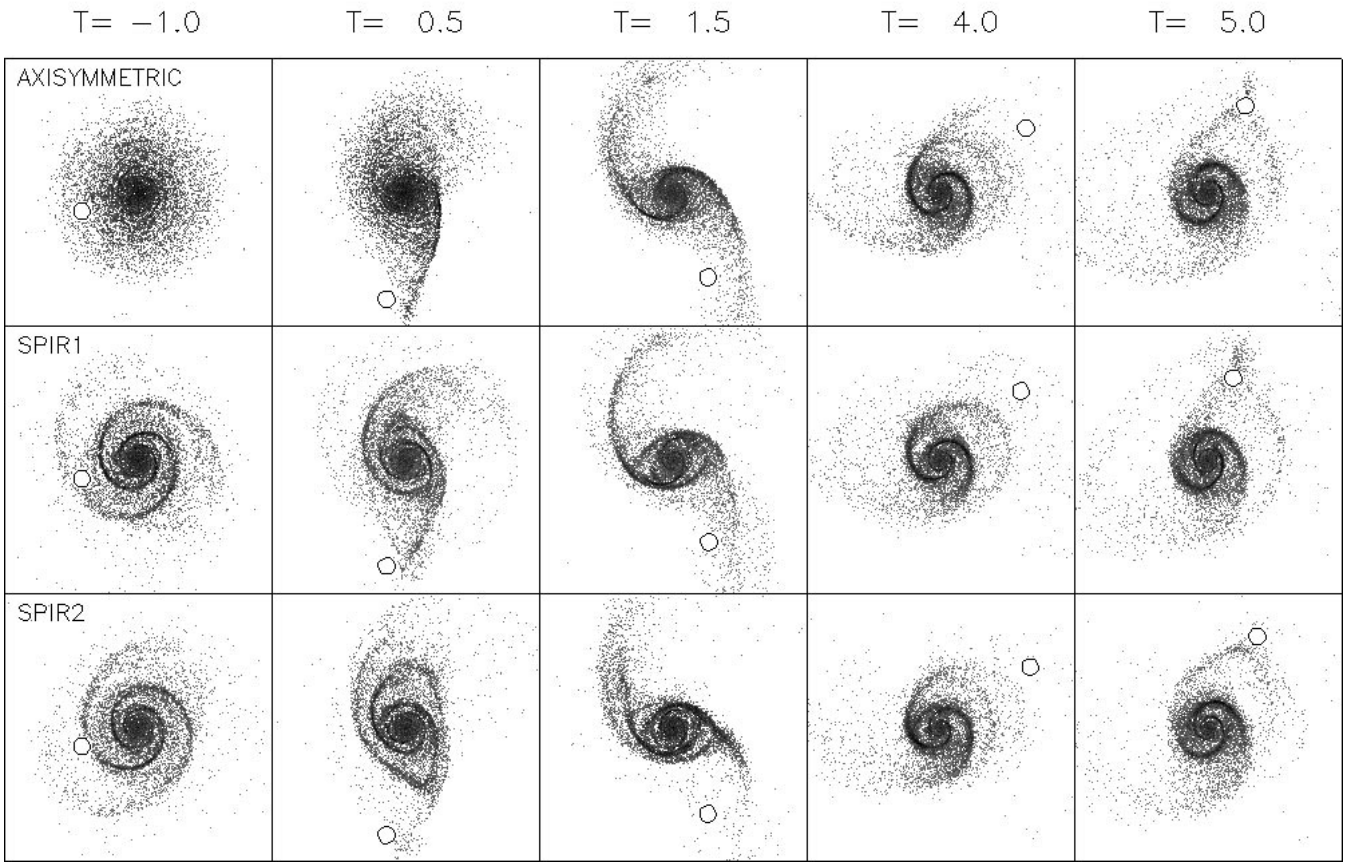

Figure 6. Influence of pre-encounter spiral structure. In the upper frames the initial disc is axisymmetric before the perturbation starts at $T = -1$. In the lower two rows the initial disc has strong pre-existing $m = 2$ spirals; these two models (SPIR1 and SPIR2) differ by 90° in the phase of the spirals. Only gas particles of the primary disc are shown, while the circle denotes the projected location of the companion.

Support for this is given also in Section 4, addressing the long-term orbital evolution.

3.4 Uncertainties in the model parameters

The above experiments have demonstrated that main observational properties of M51 can be reproduced by the multiple-passage model, including the previously unexplained kinematics of the extended tail and the high-velocity material north of the companion. As a result of various uncertainties in the modelling (e.g. unknown halo extent, orbital decay), it would be rather meaningless to attempt to derive a single set of the best model parameters. Rather, we try to estimate the parameter range for the most recent portion of the orbit ('final half-orbit'), which preserves the general properties of the model. Some complications arise since all orbital parameters are strongly correlated: any change in, say, the distance of the primary perturbation or the elapsed time, can not only affect the total strength of the perturbation, but also change significantly the location of the most current crossing.

3.4.1 Most recent disc-plane crossing ($R_{\rm down}$, $T_{\rm down}$)

We separated the effects of the most recent disc-plane crossing by experiments in which the principal perturbation was fixed to that of Fig. 1. The recent crossing was varied by allowing a slightly

Table 1. Extreme velocities in the simulations.

	Companion mass varied		
$M_{\rm p}$	$V_{\rm min}$ in Tail	$V_{\rm max}$ in North	ΔV in Tail
0.40	420	590	20
0.55	390	670	25
0.70	385	760	45
0.85	380	800	45
	Crossing distance varied		
$R_{\rm cross}$	$V_{\rm min}$ in Tail	$V_{\rm max}$ in North	ΔV in Tail
1.2	370	750	35
1.4	390	670	25
1.6	410	650	25
1.8	420	590	20

Unless otherwise mentioned, $R_{\rm cross} = 1.4$ and $M_{\rm p} = 0.55$. In all experiments $T_{\rm obs} = 6.0$, $\Omega_{\rm orb} = 345°$. Units of velocities are in $\rm km\,s^{-1}$, and they denote heliosentric recession velocities (assuming $460\,\rm km\,s^{-1}$ for the systematic velocity of the primary). Velocity range ΔV corresponds to the difference between the mean inner tail velocity at the PA $\approx 90°$ and PA $\approx 150°$. According to Rots et al. (1990) and Appleton et al. (1986), the maximum velocities in the north are about $700\,\rm km\,s^{-1}$. For the far tail, Rots et al. find a minimum velocity 360–380 $\rm km\,s^{-1}$ in its concave side, while the gradient along the continuous part of the tail is about $40\,\rm km\,s^{-1}$.

different projected velocity difference Δv between the galaxies at the best viewing time: for example, a larger Δv implies less time since the most recent crossing, and simultaneously a smaller crossing distance $R_{\rm down}$. Experiments with $R_{\rm down} \leq 1.2$ lead to an unacceptably deformed 'kink', while still closer crossings destroy the northern arm completely. On the other hand, if $R_{\rm down} > 1.4$, the effects of the second crossing remain weakly visible, but because of the longer time lapse the location of the 'kink' moves too far to the east. Thus both $R_{\rm down}$ and $T_{\rm down}$ seem to be well constrained at values near those in the previous experiments. These parameters also give the observed velocities for particles scattered to the north of the companion.

3.4.2 *Primary perturbation* ($M_{\rm p}$, $R_{\rm cross}$)

Increasing $M_{\rm p}$ or decreasing $R_{\rm cross}$ of the primary perturbation leads to more extreme velocities both for the south-east far tail and for the particles north of the companion. The simulated minimum and maximum velocities in these two regions are collected in Table 1. Passages with $M_{\rm p} < 0.55$ or $R_{\rm cross} > 1.4$ seem to be too weak to account for the observations. On the other hand, for $M_{\rm p} > 0.7$ the velocities in the north start to be somewhat too large.

The allowed direction of the primary disc crossing is rather tightly constrained in the multiple-encounter model, and follows from the projected companion location and the velocity difference. For example, if the primary crossing azimuth is pushed more to the east ($\Omega_{\rm orb} < 330°$), the orbit becomes less inclined and it is increasingly difficult to maintain a large enough velocity difference between the galaxies. Similarly, pushing the crossing azimuth toward the west ($\Omega_{\rm orb} > 360°$) implies unacceptably large Δv. The morphological fit is also best around $\Omega_{\rm orb} \approx 345°$. However, this estimate does not take into account the dynamical friction, which will shrink the orbit and thus speed up the companion even during the final half-orbit.

3.4.3 *Elapsed time since the principal perturbation* ($T_{\rm obs}$)

This parameter has a strong effect on the morphology. First, durations $T_{\rm obs} \leq 4$–5 are ruled out by the weakness of the resulting spiral structure, especially the long H I tail, as was also found in the single-passage experiments by Hernquist (1990). When $T_{\rm obs}$ is increased, the bridge morphology depends on the interplay between the most recent crossing and the spiral arms excited since the first passage. As shown above, for $T_{\rm obs} \approx 5$–6 this interplay leads to the 'kink' on the northern arm toward the companion. For a slightly longer time, $T_{\rm obs} \approx 7$, this same arm would be opened into a new bridge during the second crossing. Apparently, by increasing $T_{\rm obs}$ this process would continue with new inner arms cyclically winding to the right position and then being destroyed by the next passage. Nevertheless, as the spiral structure becomes too tightly wound, durations of $T_{\rm obs} > 6$ can be ruled out.

3.4.4 *Additional model parameters*

All the previous simulations have started at $T_{\rm start} = -1$, one time unit before the primary southern crossing. As a result of the large orbital inclination, the companion is then quite distant, about one disc radius behind the primary. Additional experiments indicate that the results are not very sensitive to the exact starting time.

Table 2. Estimated parameter range for multiple-encounter models.

$M_{\rm p}$	0.5–0.7
$R_{\rm cross}$	1.2–1.4
$T_{\rm obs}$	5.5–6.5
$\Omega_{\rm orb}$	340°–350°
$R_{\rm down}$	1.2–1.3
$T_{\rm obs} - T_{\rm down}$	0.5–1.0
$i_{\rm orb}$	75°–85°

Estimated range of uncertainty for the parameters describing the final 'half-orbit' for the M51 system. The mass ratio $M_{\rm p}$ is the companion mass relative to the total M51 mass within $4R_{\rm e}$, while $R_{\rm cross}$ is the distance of southern disc-plane crossing and $T_{\rm obs}$ the time since this crossing, occurring at azimuth $\Omega_{\rm orb}$ (counted ccw along the primary disc plane from the intersection with the sky-plane at PA = 170°). The $R_{\rm down}$ and $T_{\rm obs} - T_{\rm down}$ indicate the distance and duration since the latest crossing at north, while $i_{\rm orb}$ is the orbital inclination. The simulation length and time units equal 400 arcsec and 80×10^6 yr.

Similarly, the gross morphology and outer kinematics are not sensitive to the number of particles or the resolution of the potential evaluation. We also performed experiments with varied disc mass and scalelength. As expected, in the case of a test particle disc, the main spiral structure is very weak. On the other hand, reducing R_e reduces the scale of the spiral density waves, and the morphological resemblance to observations is lost. In both cases, the kinematics of the outer structures is only mildly affected.

3.4.5 *Final parameter range*

According to the above survey, modifications in the parameters $\Omega_{\rm orb}$, $T_{\rm obs}$, $R_{\rm down}$ as compared to those in Fig. 1 lead usually to a poorer overall fit to the observational characteristics. On the other hand, a somewhat stronger perturbation can not be ruled out, as it might even improve the kinematical properties. In conclusion, Table 2 lists tentative parameter ranges for the final 'half-orbit' of the M51 system.

4 ORBITAL DECAY

The above experiments for the M51 system suggest that at least the recent relative motion might take place along a bound low-eccentricity orbit. Direct continuation of this kind of orbit backward in time would imply several strong passages, clear signs of which would be expected to be still visible. In fact, if the above derived orbit were to be projected backward in time, the previous passages of similar strength would completely destroy the simulated structures as a result of kinematic heating of the gas disc. However, it is likely that the past orbital history has been strongly affected by the dynamical friction, so that the previous passages have been more distant and weaker. As the deceleration caused by the dynamical friction is proportional to the deformation of the primary halo and disc, in our case with a rather massive satellite, a very strong decay rate is expected.

The characteristics of the orbital decay via dynamical friction depend on the extent of the dark halo. Let us assume that the

initial relative orbit between M51 and its companion has been slightly subparabolic (see discussion in TT72) with an initial pericentre distance $R_{\rm peri}$. If the extent of the halo is small ($R_{\rm h}$ comparable to $R_{\rm peri}$), the companion feels the drag force mainly near the pericentre. As discussed in TT72 and verified by later simulations (Bontekoe & van Albada 1987), this changes mainly the orbital eccentricity, while the pericentre distance remains largely unaltered. Therefore, the tidal damage in all the previous pericentre passages would be of approximately equal strength, until the orbit as a whole would reside inside the halo, leading to a rapid merging. This was the main argument in TT72 for concluding that the present encounter must be the first pericentre passage for M51 system. However, several later studies have gathered evidence for significant extended haloes for galaxies (for a review, see e.g. Binney & Tremaine 1987). For a larger halo ($R_{\rm h} \gg R_{\rm peri}$), the drag force affects during longer portions of the orbit, and consequently both the apocentre and pericentre distances will gradually diminish (see Bontekoe & van Albada 1987) and the successive perturbations become stronger and stronger.

As in our simulations presented so far only the discs were self-gravitating, the orbital energy could not be transformed to the halo deformation and the amount of friction was thus strongly underestimated. In order to study the orbital decay more quantitatively, two different methods are employed in this section. First, we modified our simulations to include the dynamical friction with the analytical formula given by Chandrasekhar (1943). The derived current orbit can then be extended backward, assuming various models for the halo density distribution outside the visible disc. Secondly, these calculations were complemented by self-consistent live halo simulations, in which dynamical friction arises correctly via the halo deformations during the interaction.

4.1 Dynamical friction via the Chandrasekhar formula

The dynamical friction arising from the primary galaxy halo can be approximated by using the Chandrasekhar (1943) formula,

$$F_{\rm fric} = -4\pi G^2 m_{\rm p}^2 \rho \frac{\bar{v}}{v^3} F(v) \log(\Lambda), \qquad (4)$$

describing the drag force experienced by a point-mass $m_{\rm p}$ moving at speed $v = |\bar{v}|$ through an infinite homogeneous background of stars with a local density ρ. Here $F(v)$ is the fraction of background stars with speeds less than v, and the factor $\Lambda = b_{\rm max}/b_{\rm min}$, where $b_{\rm max}$ and $b_{\rm min}$ are the maximum and minimum impact parameters. For an unperturbed, infinite isothermal sphere with a constant circular speed $v_{\rm c}$,

$$F(v) = \phi(v/v_{\rm c}) - v/v_{\rm c} \quad \phi'(v/v_{\rm c}), \qquad (5)$$

where ϕ denotes the error function and ϕ' its derivative (Tremaine 1976). Here we assume that the above formulae are approximately valid also for the extended companion moving inside the truncated halo of the primary galaxy. The choice of the maximum and minimum impact parameters is rather arbitrary: following Tremaine (1976) we use $b_{\rm max} = |R_2 - R_1|$, the distance between the halo centres. To reflect the extended size of the companion we take $b_{\rm min} = \max[r_{\rm comp}, Gm_{\rm p}/v^2]$, where $r_{\rm comp}$ is the median radius of the companion and the other quantity in brackets represents the minimum impact parameter for a pointmass.

Fig. 7 displays three examples of the orbital decay obtained by including the above drag force on the equation of motion for the companion. The difference between the cases is that the outer truncation radius of the halo of M51 has been varied between 2–4 distance units (corresponds to 8–16 disc scalelengths). In each case, the increase of $R_{\rm h}$ is accompanied by a corresponding increase in the total $M_{\rm halo}$, however keeping the halo to-disc-mass ratio (2:1) unaffected within the disc radius, the total $M_{\rm halo}/M_{\rm disc}$ being 4–8. The orbits have been chosen so that their final portions correspond to the nominal model of the previous section, and thus match the constraints of the location and velocity of the present companion. In the case of a relatively small halo ($R_{\rm h} = 2$), the main characteristic of the orbital evolution is indeed the decay of the eccentricity while the pericentre distances stay almost constant, as expected. Thus the previous perturbations were only slightly weaker than the principal perturbation at $T = 0$. As a result, the extended tail appears considerably more dispersed than in the models of Section 3. For the other two models with larger $R_{\rm h}$, the previous passages occur at larger distances thus reducing the previous tidal damage considerably. In the model with $R_{\rm h} = 4$, the effects of the previous passages on the final morphology are almost negligible, the extended tail being also very similar to that in the nominal model of Section 3.

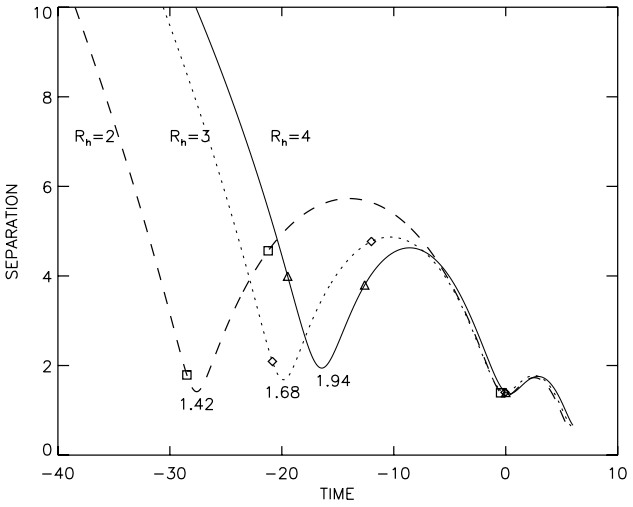

Figure 7. Primary galaxy and companion separation versus time in simulations including the Chandrasekhar formula for dynamical friction. The companion was modelled only by a halo, with mass 0.55, feeling the drag force according to equation (4). Three experiments with $R_{\rm h} = 2$, 3, and 4 are shown, with total halo masses $M_{\rm h} = 1.33$, 2.00 and 2.67, respectively. The numbers below the curves indicate in each case the distance of the previous pericentre passage, while squares indicate the time of disc crossings. As before, $T \approx 0$ corresponds to the southern disc plane crossing.

The dependence of the outer disc heating on the distance of the previous passages is illustrated in Fig. 8, showing the time evolution of the velocity dispersion of the gas particles at various distances. According to Fig. 8, the previous perturbation in the model with $R_{\rm h} = 2$ increases the velocity dispersion by almost a factor of 3. As the cooling via collisions is inefficient in the low-density outer regions, $\sigma_{\rm r}$ remains at a high level when the primary perturbation occurs at $T = 0$. The inner parts cool more efficiently so that the final morphology of the inner disc is less affected. Only for the model with $R_{\rm h} = 4$, the perturbation-induced increase of random velocities is negligible in all parts of the gas disc. Similar behaviour takes place also for the stellar component, except that the increase of velocity dispersion is irreversible.

The above examples suggest that the existence of a well-defined

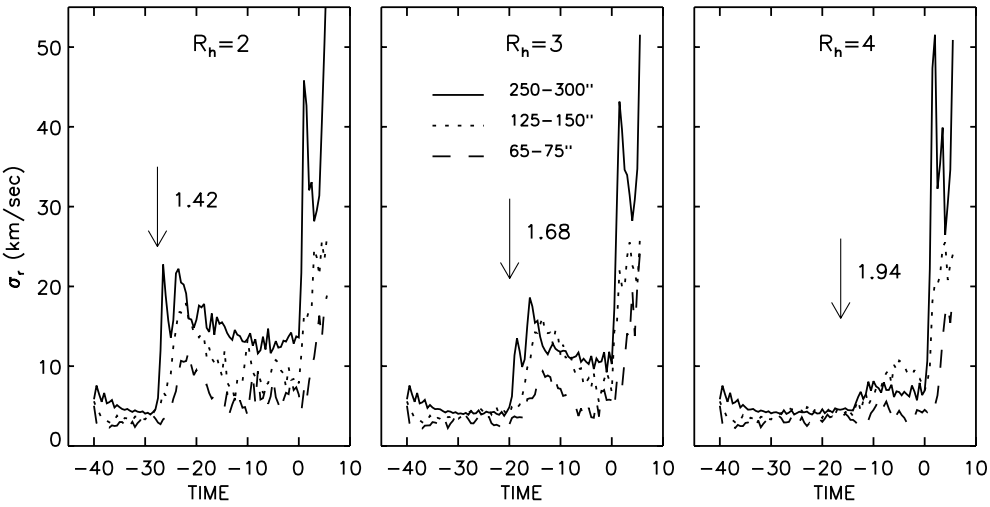

Figure 8. Evolution of the gas radial velocity dispersion in the experiments in Fig. 7, shown separately for three circular zones. The arrows mark the time of the previous pericentre passage, occurring before $T = 0$, and the number gives the corresponding distance.

Table 3. Halo models in self-consistent simulations.

MODEL	W_0	r_0	$M_{\rm tot}$	M_5	$N_{\rm part}$
A	6	0.5	1.00	1.00	80 000
B	7.5	0.5	1.75	1.52	140 000
C	12.0	0.75	5.20	2.34	205 000

King models for haloes are characterized by the dimensionless central potential W_0 and King radius r_0 (Binney & Tremaine 1987). $M_{\rm tot}$ and M_5 denote the total halo mass and mass within 5 simulation units, respectively. $N_{\rm part}$ is the number of halo particles. In each case the bulge was described with a King model with $W_0 = 3$, $r_0 = 1/16$, $M_{\rm b} = 1/32$, realized with 5000 particles. The exponential disc had $r_{\rm e} = 0.25, M_{\rm disc} = 0.333$ and $N_{\rm star} = 100\,000$. Gravity softening was 0.05 simulation units, while the grid size was extended by using $N_{\rm rad} = 60$, covering distances up to 80 simulation units. In the case of Model C, the initial halo was truncated at 15 simulation units, and the values correspond to those actually employed in simulations.

extended tail requires that the minimum distance of the previous close passages has been at least about 30 per cent larger than the principal perturbation in the south. This seems to be possible, provided that M51 has an extended halo with ~10 times the disc mass. However, the validity of the Chandrasekhar formula for galaxy encounters has its limitations, as discussed for example by Barnes (1998). Therefore, to check the previous experiments, simulations with live haloes were also performed.

4.2 Self-consistent simulations

In self-consistent runs, the analytical halo potential of the primary galaxy was replaced by a self-gravitating halo and bulge particles. The simulation method was essentially similar to that used in the previous runs: the 3D density table now included also the contribution from the halo and bulge particles, and the forces affecting them were calculated by an interpolation from the 3D force tables. For simplicity, the companion was described by an analytical force model (isothermal sphere with $m_{\rm p} = 0.55$), and its disc was ignored. The main technical difference from the simulations with an analytical halo is in the centring of the potential grid of the main galaxy, which is now placed at the local minimum of the gravitational potential. This minimum is searched at each step by an iteration process, which converges in just a few iterations. The validity of the simulation method was checked against tree-code simulations involving collision of Plummer spheres (tree-code simulations were performed by the program kindly provided by L. Hernquist; TREECODE version 3).

The setting-up of the initial bulge + halo + disc models follows the method of Barnes (1988). King models with different degrees of central concentration are used for both the bulge and the halo, and the initial velocity distribution is solved from the phase-space distribution of each component separately. Bulge and halo are allowed to relax in combination for five crossing times, after which an analytical disc potential is introduced, corresponding to the exponential disc, slowly increasing in strength for 10 crossing times. The analytical disc is then replaced by disc particles, with their velocities calculated with the epicyclic approximation, as in Section 2. The combined bulge + disc + halo system is then allowed to relax in isolation for an additional 10 crossing times, before the companion is introduced. During this initial setting-up process, considerable evolution of the halo mass distribution takes place, mainly as a result of relaxation against the other components, and to a smaller degree because of the use of softened forces. After some experimentation, three different Models A–C (see Table 3) were constructed, each corresponding to a different halo concentration and total mass (total $M_{\rm halo}/M_{\rm disc}$ between 3 and 15), but still possessing a rotation curve which for $R = 100 - 400$ arcsec is fairly similar to that of the analytical halo models studied in the previous subsection (see Fig. 9).

A brief orbital survey was performed, concentrating on parabolic and subparabolic initial orbits with different initial pericentre distances (Fig. 10). No attempt was made to match the projected separation and velocity difference of the M51 pair: the main objective was to check that the distances of the successive passages can indeed decrease in a manner that retains the gas disc as dynamically cool before the latest two disc crossings studied in Section 3. In each experiment, the initial orbital plane of the companion was perpendicular to the primary disc. In the uppermost row of Fig. 10, five simulations for Model

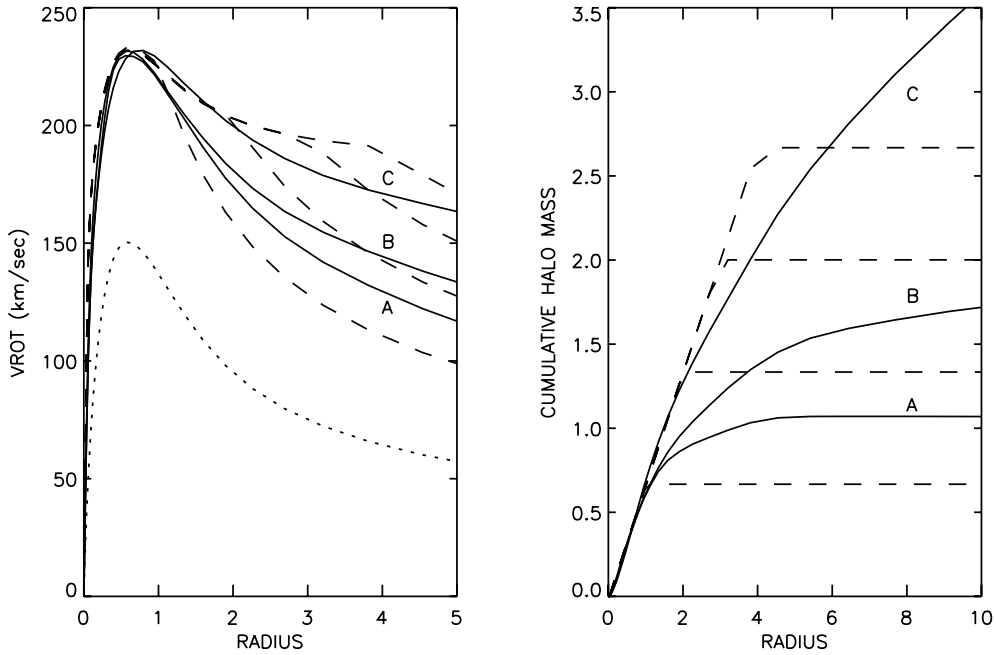

Figure 9. Rotation curves and mass models in self-consistent simulations. In the left-hand panel, solid lines denote the total circular velocity curves of live halo Models A–C. Dashed lines indicate analytical halo models studied with Chandrasekhar's formula, while dotted line indicates the disc contribution. In the right-hand panel, the cumulative halo mass is shown for the same models (includes bulge contribution).

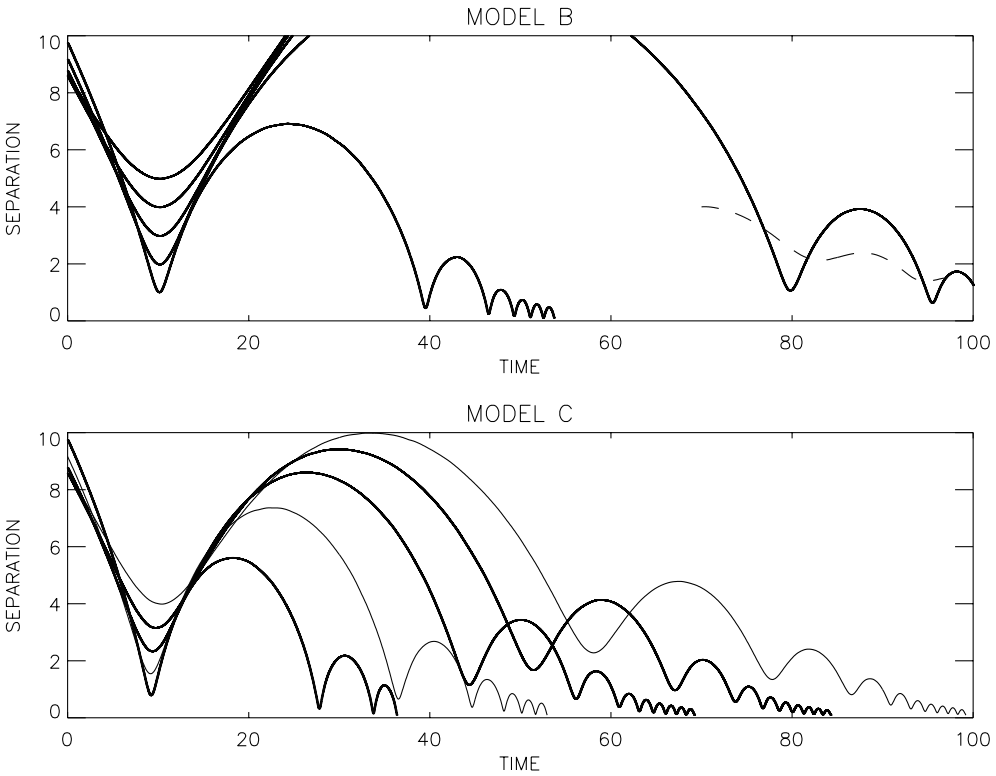

Figure 10. Orbital decay in simulations with self-consistent haloes. In the upper frame initially parabolic orbits are studied for Model B, each having 90° inclination with respect to the disc plane of the primary. Initial pericentre passages occur at distances of 1–5 simulation units. In the lower frame, the same initial velocity vectors are used with a more massive halo, Model C. Simulations were terminated when the distance between the components became less than 0.2 distance units: however, the method of using rigid potential for the companion becomes unreliable even before this, accounting for the unrealistic regular small oscillations in the final portions of the orbit. The dashed line in the upper frame corresponds to the orbit in the simulation of Fig. 11.

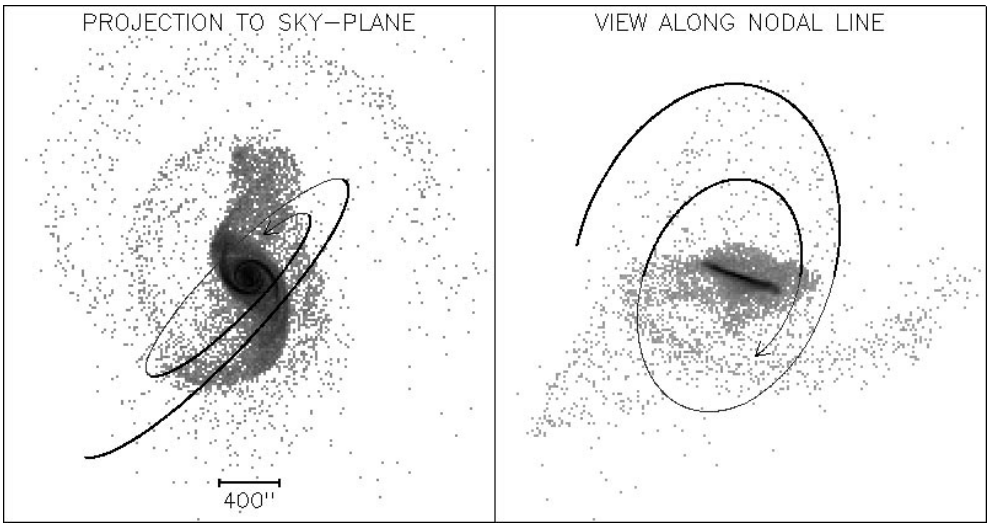

Figure 11. Self-consistent simulation example for M51, including several disc plane crossings. The gas component is shown from two different viewing directions. Model B was used for the halo and 40 000 gas particles were used. The orbit is also displayed in Fig. 10.

B are displayed: in the absence of dynamical friction they would correspond to parabolic orbits, with pericentre distances of 1–5 simulation units. Only two of these orbits (with $R_{\rm peri} \leq 2$) experience enough orbital drag from dynamical friction to lead to another close passage during the studied time interval of 100 crossing times ($\approx$8 Gyr). The other frame shows the evolution for Model C, starting with the same initial velocity vectors. As a result of the deeper potential well, the initial orbits are now slightly subparabolic, with the initial apocentre distances corresponding to about 25–30 distance units. Now the orbital decay is stronger, leading in all studied cases to an eventual merging. With a sufficiently large initial pericentre distance, this model allows orbits that on their evolved portions resemble those derived in the previous subsection, with a gradual decrease of both the pericentre and apocentre. This seems to confirm that the low eccentricity current orbit assumed in Section 3 is indeed possible.

In general, it is very difficult to find a good final match with M51, starting from an initially extended orbit and following its shrinking for several revolutions. One fortuitious example is displayed in Fig. 11. This simulation used Model B for the primary halo, and the companion was started from an already low eccentricity orbit, from a distance of 4 simulation units. In this simulation, the companion crosses the disc plane of the primary altogether four times, the last crossing matching roughly the most recent passage implied by the models in Section 3. The overall morphology mimics M51 rather well, and the projected companion location and velocity are not far from the observed values ($\Delta v = 105\,{\rm km\,s^{-1}}$). The extended tail is also formed, and displays the apparent counter-rotating motion. Interestingly, there are also fainter more extended structures, being relics of the previous more distant passages. Most importantly, this experiment and the previous orbital models have shown that with large enough haloes, multiple encounters may occur without heating the disc too much to produce the present characteristics of M51.

5 SUMMARY AND DISCUSSION

The dynamics of the M51 system has been investigated with a large number of self-gravitating simulation experiments. This survey was carried out with a 3D multiple spherical polar grid code, where both components of the pair are described with self-gravitating discs embedded in inert analytical haloes. Both stars and gas were included, gas being described by dissipatively colliding particles. An important advantage in our method was the use of the orbital fitting procedure described in SL93: we were able to start our *N*-body experiments with initial values which lead to orbits passing through the observed companion location with the observed line-of-sight velocity difference. In this manner it was possible to study systematically the different perturbation strengths and durations.

Two possible classes of current orbits were found, both matching the present morphology rather well: either nearly parabolic single passages, or bound encounter orbits enabling the companion to cross the plane of the primary disc several times. In the bound model, the deeply penetrating spiral structure is induced during a passage toward the observer in the south (PA $\approx$ 155°), at a distance of about 25–30 kpc, and about 400–500 Myr ago. The latest passage took place about 50–100 Myr ago. In this model, the current position of the companion is less than 20 kpc behind the primary galaxy. In the near-parabolic single-passage model, resembling the latest model by Toomre (1995), the passage occurred in the south, again about 400–500 Myr ago, but roughly in the opposite direction as compared to the bound model. In this model the current location of the companion is far behind the disc of M51.

An important result of our study is that the major kinematical observations of M51 can be accounted for. The bound model explains, not only the overall velocity field of the disc of M51, but also the apparent counter-rotation of the H I tail, which is tilted by 40°–50° with respect of the inner disc. It also explains the high gas velocities up to $700\,{\rm km\,s^{-1}}$ to the north of the companion. The main morphological features were produced also by the nearly parabolic model, but it fails to yield the above kinematical properties. The recent passage in the bound model can also be related to some morphological characteristics as the observed 'kink' in the northern spiral arm of M51, not produced by the single-encounter model.

Both disc crossings on the bound orbit contribute to the out-of-plane velocities of the tail particles, which acquire inclined orbits

with respect to the inner disc. In our model for the M51 system, the extended H I tail is composed mainly of particles originating from the initial bridge formed during the southern crossing. These particles, after completing almost a full orbital period, are again moving toward the observer. The particles in the original tail end up in the same south-east region, which might be relevant for the observed structure of the tail, showing some weak signs of a double structure (see fig. 1 in Rots et al. 1990). In the major axis rotation curve, the out-of-plane velocities manifest as an S-shaped structure, leading to an apparent decline even if the actual rotation curve stays close to the initially assumed flat rotation curve. This contrasts to Elmegreen & Thomasson (1993), who argued that the S-shaped rotation curves, typical for interacting galaxies, are signs of small haloes. On the other hand, our result is consistent with the recent study of Barton, Bromley & Geller (1999), who show that interaction-induced transient velocities may lead to either a fall or a rise of the observed rotation curve, depending on the viewing direction.

The main characteristics of the companion were also roughly reproduced by the model: the companion developed a bar, the outer parts of its intensity profile flattened during the encounter, and long faint tidal extensions were developed, pointing roughly to the observed directions. As explained in Section 1, the direction of these extensions was a problem in the recent model by Toomre (1995). However, in the current models they appeared to be fairly similar to those in TT72, which is not suprising taking into account that our companion orientation and initial extent, as well as the direction of the latest crossing, are fairly similar to the TT72 model.

Following the suggestion in Lin & Bertin (1995), we also performed experiments in which the M51 disc had a strong spiral structure before the current perturbation. The final morphology in these simulations was practically indistinguishable from the runs started from nearly axisymmetric initial states. This seems to indicate that a strong perturbation may temporarily overwhelm pre-existing patterns, in contrast with the view in Lin & Bertin (1995).

The possible origin of the bound current orbital configuration was studied via simulations including dynamical friction, calculated with Chandrasekhar's (1943) analytical formula for the drag force felt by the companion while moving inside an extended halo of the primary galaxy. The survey was constrained to orbits the last portions of which were similar to those in our multiple-encounter model. According to these experiments, an initially nearly parabolic orbit can be transformed into a low-eccentricity orbit, even for a fairly modest massive halo. The existence of the well-defined H I tail suggests that the previous close passages must have been at least about 30 per cent more distant than the southern crossing. This prevents excessive dynamical heating of the outer parts of the gas disc, so that a fairly narrow extended tail can form during the last 500 Myr. In our experiments with truncated constant circular velocity haloes, sufficiently fast shrinking of the orbit was achieved in models containing a total mass of a few times that inside the disc region (total $M_{\rm halo}/M_{\rm disc} > 10$). Somewhat analogous reasoning was presented by Tremaine (1976) in support of the extended halo of our Galaxy: he argued that the Magellanic cloud system broke up only at their latest perigalactic passage, indicating that significant orbital shrinking had taken place since the previous pericentre passage. The above results with the Chandrasekhar formula were also checked with experiments using a self-consistent halo described by self-gravitating particles. Simulation examples with live haloes yielded a good overall match in morphological and kinematical properties even after four disc-plane crossings.

Admittedly, our brief survey of extended haloes was far from complete, being limited to models in which the rotation curve was slightly declining beyond the disc region, and whose total halo mass was fairly moderate. In these models there was no difficulty in forming an extended tail similar to the H I tail of M51. Recently, Dubinski, Mihos & Hernquist (1999) have carried out an extended survey of the effects of the halo density profile on the formation of tidal tails. According to their study, massive extended flat-rotation curve haloes, as suggested by currently favoured cosmological models, should be fairly effective in supressing the tail formation, at least in close parabolic encounters. Clearly, the success of forming the extended tail could thus be very model-dependent. However, there is no discrepancy with the Dubinski et al. (1999) results, since our tail was formed only in the advanced stages of the orbital evolution, when a significant amount of orbital circularization had already taken place. For more extended haloes, the efficiency of this process could be expected to be even stronger. Also, the extended tail of M51, spanning about 10 disc scalelengths, is rather modest compared to systems like Antennae and Superantennae receiving the main attention in Dubinski et al. (1999).

Our simulation models support the view that the main spiral structure of M51 may be explained by tidally induced, transient density waves like those envisaged by TT72. Likely candidates for their formation are (1) forcing by the strongly deformed outer parts (Toomre 1969, TT72) and/or (2) the direct *in situ* amplification of tidally induced kinematic waves by the swing amplification process (Toomre 1981). The analysis of the simulated spiral patterns, and their dependence on the orbital and disc properties, will be presented in Paper II, employing simulations with larger particle numbers and improved gravity resolution.

ACKNOWLEDGMENTS

We thank the referee, Dr J. Dubinski, for his useful suggestions. The support from the Academy of Finland is acknowledged.

REFERENCES

Appleton P. N., Foster P. A., Davies R. D., 1986, MNRAS, 221, 393
Barnes J., 1988, ApJ, 331, 699
Barnes J., 1998, in Friedli D., Martinet L., Phenniger D., eds, Galaxies: Interactions and Induced Star Formation. Springer, Heidelberg, p. 275
Barton E. J., Bromley B. C., Geller M. J., 1999, ApJ, 511, L25
Binney J., Tremaine S., 1987, Galactic Dynamics. Princeton Univ. Press, Princeton, NJ
Bontekoe Tj., van Albada T. S., 1987, MNRAS, 224, 349
Burkhead M. S., 1978, ApJS, 38, 147
Byrd G., Salo H., 1995, Astrophys. Lett. Commun., 31, 193
Chandrasekhar S., 1943, ApJ, 97, 255
Dubinski J., Mihos J. C., Hernquist L., 1999, ApJ, 526, 607
Elmegreen B. G., Thomasson M., 1993, A&A, 272, 37
Elmegreen B. G., Elmegreen D. M., Seiden P. E., 1989, ApJ, 343, 602
Ford H. C., Crane P. C., Jacoby G. H., Lawrie D. G., van der Hulst J. M., 1985, ApJ, 293, 132
Hernquist L., 1990, in Wielen R., ed., Dynamics and Interactions of Galaxies. Springer, Heidelberg, p. 108
Lin C. C., Bertin G., 1995, Ann. New York Acad. Sci., 773, 125
Lin C. C., Shu F., 1964, ApJ, 140, 646
Moss D., Rautiainen P., Salo H., 1999, MNRAS, 303, 125
Persic M., Salucci P., 1990, MNRAS, 245, 577

Rand R. J., 1993, ApJ, 410, 68
Rots A. H., Bosma A., van der Hulst J. M., Athanassoula E., Crane P. C., 1990, AJ, 100, 387
Salo H., 1991, A&A, 243, 118
Salo H., Byrd G., 1994, in Shlosman I., ed., Mass Transfer Induced Activity in Galaxies. Cambridge Univ. Press, Cambridge, p. 412
Salo H., Laurikainen E., 1993, ApJ, 410, 586 (SL93)
Salo H., Laurikainen E., 2000, MNRAS, 319, 393 (Paper II, this issue)
Salo H., Rautiainen P., Buta R., Purcell G., Cobb M., Crocker D., Laurikainen E., 1999, AJ, 117, 792
Schweizer F., 1976, ApJS, 31, 313
Schweizer F., 1977, ApJ, 211, 324
Scoville N., Young J. S., 1983, ApJ, 265, 148
Shu F. H., Stachnik R. V., Yost J. C., 1971, ApJ, 166, 465
Smith J., Gehrz R. D., Grasdalen G. L., Hackwell J. A., Dietz R. D., Friedman S. D., 1990, ApJ, 362, 455
Spillar E. J., Oh S. P., Johnson P. E., Wenz M., 1992, AJ, 103, 793
Spitzer L., 1942, ApJ, 95, 329
Thronson H. A., Rubin H., Ksir A., 1992, MNRAS, 252, 550
Tilanus R. P. J., Allen R. J., 1991, A&A, 244, 8
Toomre A., 1969, ApJ, 158, 899
Toomre A., Toomre J., 1972, ApJ, 178, 623 (TT72)
Toomre A., 1981, in Fall S. M., Lynden-Bell D., eds, The Structure and Evolution of Normal Galaxies. Cambridge Univ. Press, Cambridge, p. 111
Toomre A., 1995, lecture given at Instituto de Astronomia, UNAM, 1995 April
Tremaine S. D., 1976, ApJ, 203, 72
Tully R. B., 1974a, ApJS, 27, 415
Tully R. B., 1974b, ApJS, 27, 437
Tully R. B., 1974c, ApJS, 27, 449
Zang T. A., 1976, PhD thesis, Massachusetts Institute of Technology, Cambridge MA
Zaritsky D., Rix H., Rieke M., 1993, Nat, 364, 313

This paper has been typeset from a TEX/LATEX file prepared by the author.